Nano Research
2022, 15(12): 10063–10069

ISSN 1998-0124 CN 11-5974/O4
https://doi.org/10.1007/s12274-022-4467-3

Research Article

Axial coordination regulation of MOF-based single-atom Ni catalysts by halogen atoms for enhanced CO_2 electroreduction

Jia-Xin Peng[1], Weijie Yang[2], Zhenhe Jia[2], Long Jiao[1] (✉), and Hai-Long Jiang[1] (✉)

[1] *Department of Chemistry, University of Science and Technology of China, Hefei 230026, China*
[2] *Department of Power Engineering, School of Energy, Power and Mechanical Engineering, North China Electric Power University, Baoding 071003, China*

Received: 31 March 2022 / **Revised:** 20 April 2022 / **Accepted:** 21 April 2022

ABSTRACT

Single-atom catalysts (SACs), with the utmost atom utilization, have attracted extensive interests for various catalytic applications. The coordination environment of SACs has been recognized to play a vital role in catalysis while their precise regulation at atomic level remains an immense challenge. Herein, a post metal halide modification (PMHM) strategy has been developed to construct Ni-N_4 sites with axially coordinated halogen atoms, named Ni_1-N-C (X) (X = Cl, Br, and I), on pre-synthetic nitrogen-doped carbon derived from metal–organic frameworks. The axial halogen atoms with distinct electronegativity can break the symmetric charge distribution of planar Ni-N_4 sites and regulate the electronic states of central Ni atoms in Ni_1-N-C (X) (X = Cl, Br, and I). Significantly, the Ni_1-N-C (Cl) catalyst, decorated with the most electronegative Cl atoms, exhibits Faradaic efficiency of CO up to 94.7% in electrocatalytic CO_2 reduction, outperforming Ni_1-N-C (Br) and Ni_1-N-C (I) catalysts. Moreover, Ni_1-N-C (Cl) also presents superb performance in Zn-CO_2 battery with ultrahigh CO selectivity and great durability. Theoretical calculations reveal that the axially coordinated Cl atom remarkably facilitates *COOH intermediate formation on single-atom Ni sites, thereby boosting the CO_2 reduction performance of Ni_1-N-C (Cl). This work offers a facile strategy to tailor the axial coordination environments of SACs at atomic level and manifests the crucial role of axial coordination microenvironments in catalysis.

KEYWORDS

metal–organic frameworks, single-atom catalysts, CO_2 electroreduction, axial coordination environment

1 Introduction

Single-atom catalysts (SACs), featured with isolated metal atoms dispersed on supports, present unprecedented activity and selectivity for various reactions and have become the frontier of heterogeneous catalysis [1–10]. Single metal atoms in SACs, with extremely high specific surface energy, are usually stabilized via coordination interaction by suitable supports [11, 12]. Thereby, the catalytic performance of SACs is significantly affected by their local coordination environments [13–15]. Taking CO_2 electroreduction as an example, it suffers from low efficiency due to chemical inertia of CO_2 and the competing hydrogen evolution, and the decrease of coordination number for single-atom Ni catalysts has been widely proved to alleviate these challenges [16–18]. On account of this, regulating the coordination environments of SACs precisely will be of great significance for catalytic performance optimization and mechanism investigation [19–22].

To be specific, single metal atoms implanted nitrogen-doped carbon (M-N-C) catalysts, one of the most important SACs, are usually identified to possess porphyrin-like planar M-N_4 sites dominantly [23, 24]. However, the high electron/structure symmetry of M-N_4 sites is unfavorable for the charge transfer during catalysis, hindering the further performance optimization of M-N-C catalysts [25]. To break the symmetric electronic structure of single-atom metal sites, a series of coordination environment regulation strategies, such as changing coordination numbers and replacing some of the coordinated nitrogen atoms by other heteroatoms, have been developed and greatly enhanced the catalytic performance of M-N-C catalysts [17, 26–28]. Unfortunately, these regulations are all limited in the carbon plane and unavoidably change the properties of carbon support in the meantime [29, 30]. The axial coordination environment regulation, which can be performed out of carbon support plane, should be an ideal way to optimize the catalytic performance of SACs without influencing the properties of carbon support [31]. Although great progress has been achieved in the precise construction of SACs, the axial coordination environment regulation remains a grand challenge [25, 32, 33].

Metal–organic frameworks (MOFs) [34–37], as a class of crystalline porous material with tunable components and structure, exhibit great research prospects in diverse fields [38–43]. In recent years, MOFs have been regarded as one of the most auspicious candidates for the accurate construction of SACs [44, 45]. Thanks to the flexible structure and composition, MOFs also show great advantages on the coordination environment regulation of single-atom sites via one-step pyrolysis [29, 46]. However, due to the uncontrollability of

Address correspondence to Long Jiao, longjiao@ustc.edu.cn; Hai-Long Jiang, jianglab@ustc.edu.cn

pyrolysis process, traditional one-step pyrolysis of MOFs is still difficult to control the axial coordination of SACs accurately [33]. Inspired by post-metallization strategy for the construction of metal porphyrin complexes, the axial coordination atoms can be easily adjusted by selecting metal salts with different anions [47]. Following this synthesis route, the post insertion of single atoms on MOF-derived nitrogen-doped carbon, which can decouple the carbon support preparation and subsequent single metal atom decoration, should be an ideal way to regulate the axial coordination environments of SACs.

With this in mind, a facile post metal halide modification (PMHM) strategy has been developed to decorate single Ni atoms with different axial halogen atoms (Cl, Br, and I) on the pre-fabricated nitrogen-doped carbon derived from ZIF-8 (ZIF = zeolitic imidazolate framework). During the pyrolysis of ZIF-8, metallic Zn converted from Zn^{2+} can evaporate away due to the low boiling point, leaving nitrogen-doped porous carbon (N-C). The abundant nitrogen atoms of N-C can serve as anchoring sites to coordinate with NiX_2 salts (X = Cl, Br, and I), obtaining a series of single-atom Ni sites coordinated by four nitrogen atoms and an axial halogen atom (denoted as Ni_1-N-C (X), X = Cl, Br, and I) (Fig. 1). The Ni_1-N-C (Cl) catalyst, with the most electronegative Cl atoms modified in the axial direction, exhibits ultrahigh Faradaic efficiency (FE) of CO up to 94.7%, much superior to Ni_1-N-C (Br) and Ni_1-N-C (I). Theoretical simulations unveil that the single-atom Ni site with axial Cl atom can accelerate the formation of *COOH and greatly promote the CO_2 reduction process of Ni_1-N-C (Cl).

2 Results and discussion

A representative Zn-MOF, ZIF-8 also named as MAF-4 [48, 49], was prepared by self-assembly of Zn^{2+} and 2-methylimidazole in methanol (Fig. S1 in the Electronic Supplementary Material (ESM)). The typical type-I N_2 sorption isotherms exhibit the microporous characteristic of ZIF-8 with a large surface area of 1,331 m^2/g (Fig. S2 in the ESM). As can be seen from scanning electron microscopy (SEM) and transmission electron microscopy (TEM) images, the as-synthesized ZIF-8 presents a rhombic dodecahedral morphology with an average size of 80 nm (Figs. 2(a) and 2(b)). Through the direct pyrolyzation of ZIF-8 at 900 °C, N-C with well-retained morphology as ZIF-8 can be obtained (Fig. 2(c) and Fig. S3 in the ESM). After being refluxed in the solution of nickel chloride, the N-C with abundant N coordination sites can be easily decorated by Ni atoms, forming the Ni_1-N-C (Cl) catalysts with Ni loading of 0.64 wt.% and N content of 6.25 wt.% (Table S1 in the ESM). Following this method, Ni_1-N-C (Br) and Ni_1-N-C (I), with comparable Ni loading and N content to Ni_1-N-C (Cl), have also been fabricated by the adoption of nickel salts with different halogen anions (Table S1 in the ESM).

Taking Ni_1-N-C (Cl) as an example, it shows inherited morphology and particle size of N-C (Figs. 2(c)–2(e) and Fig. S3 in the ESM). No obvious nanocrystals or nanoparticles can be observed in the TEM image of Ni_1-N-C (Cl), manifesting the atomic dispersion of Ni (Fig. 2(e)). Moreover, the powder X-ray diffraction (XRD) pattern of Ni_1-N-C (Cl) only presents two broad peaks corresponding to the (002) and (101) planes of carbon and no crystalline species of Ni is detected, in accordance with TEM observation (Fig. S4 in the ESM and Fig. 2(e)). Raman spectrum of Ni_1-N-C (Cl) displays two peaks at 1,339 and 1,578 cm^{-1}, which can be ascribed to the disorder (D band) and graphitic (G band) carbon, respectively (Fig. S5 in the ESM). The intensity ratio of D band to G band (I_D/I_G) for Ni_1-N-C (Cl) is calculated to be 1.04, showing the similar graphitization degree to N-C (Fig. S5 in the ESM). Furthermore, Ni_1-N-C (Cl) exhibits a large surface area (633 m^2/g) with highly porous structure similar to that of N-C, which favors the dispersion of catalytic center atoms and would expedite mass transfer during catalysis (Fig. S6 in the ESM). Meanwhile, Ni_1-N-C (Br) and Ni_1-N-C (I) are also characterized and present similar morphology, graphitization degree, and porous structure to those of Ni_1-N-C (Cl) (Figs. S4–S7 in the ESM and Figs. 2(d) and 2(e)).

To identify the chemical compositions and element electronic states of Ni_1-N-C (X) (X = Cl, Br, and I), X-ray photoelectron spectroscopy (XPS) is further conducted. The Ni $2p_{3/2}$ peaks in Ni_1-N-C (X) (X = Cl, Br, and I) exhibit the decreased binding energy in the sequence of Ni_1-N-C (Cl), Ni_1-N-C (Br), and Ni_1-N-C (I), which can be ascribed to the decreasing electronegativity from Cl to I (Fig. 3(a)). This manifests the higher oxidation state of Ni in Ni_1-N-C (Cl) than those in Ni_1-N-C (Br) and Ni_1-N-C (I). Additionally, it should be noted that the peak at 875.2 eV overlapping with Ni $2p_{1/2}$ in Ni_1-N-C (I) catalyst is the signal of I $3p_{3/2}$ (Fig. 3(a)) [50]. The N 1s spectra of Ni_1-N-C (X) (X = Cl, Br, and I) can be deconvoluted into five characteristic peaks, and the existence of metal-N species, attributed to the empty orbitals of metal atoms accepting the lone pair electrons of N atoms, clearly indicates the formation of Ni–N coordination bonds (Figs. S8(a)–S8(c) and Fig. S9 in the ESM) [51]. Furthermore, the existence of halogen atoms in the three obtained catalysts is also confirmed by XPS measurements. The Cl 2p XPS spectrum of Ni_1-N-C (Cl) presents a peak at 197.7 eV, manifesting the formation of Ni-Cl coordination (Fig. S8(d) in the ESM) [52]. Moreover, the peaks at 68.0 and 68.9 eV in the Br 3d XPS spectrum of Ni_1-N-C (Br) and the peaks located at 619.2 and 630.7 eV in the I 3d spectrum of Ni_1-N-C (I) verify the existence of Ni-Br and Ni-I coordination, respectively (Figs. S8(e) and S8(f) in the ESM) [53, 54]. The aberration-corrected high-angle annular dark-field scanning transmission electron microscopy (HAADF-STEM) image of Ni_1-N-C (Cl) illustrates isolated bright spots dispersed on

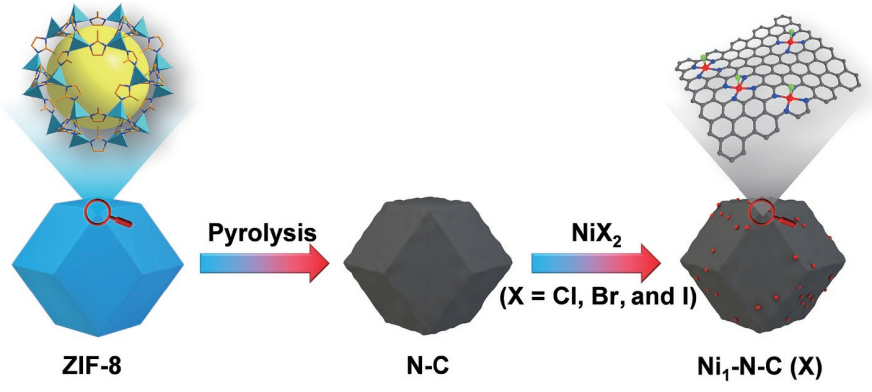

Figure 1 Illustration for the construction of Ni_1-N-C (X) (X = Cl, Br, and I) single-atom catalysts via a PMHM strategy.

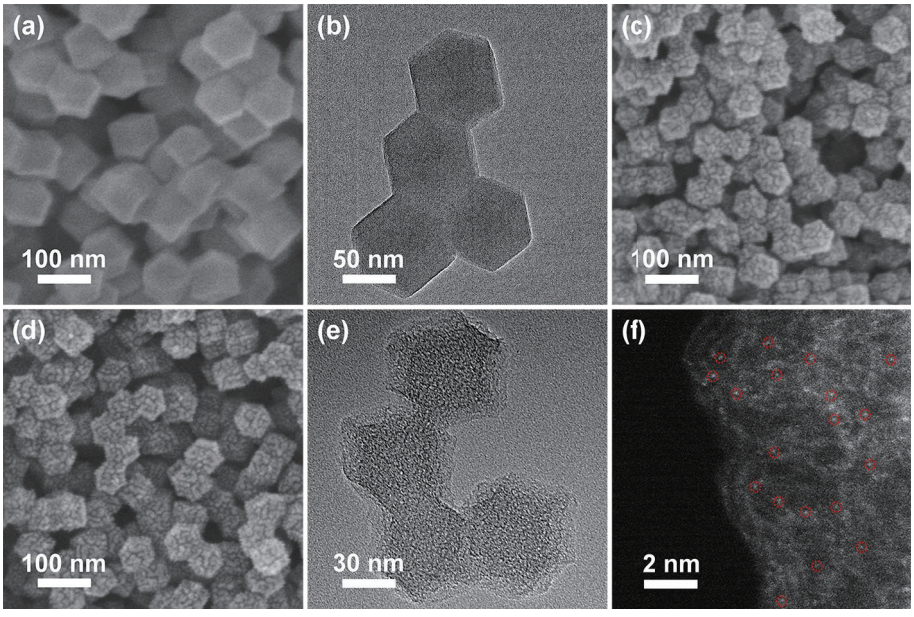

Figure 2 (a) SEM and (b) TEM images of ZIF-8. (c) SEM image of N-C. (d) SEM, (e) TEM, and (f) aberration-corrected HAADF-STEM image of Ni_1-N-C (Cl).

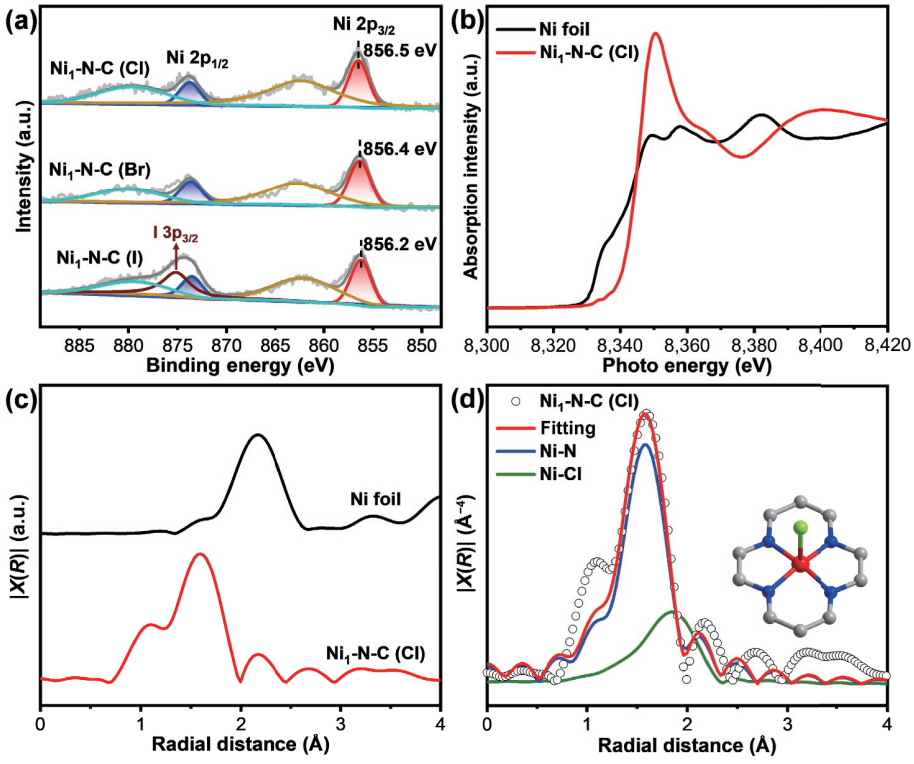

Figure 3 (a) The Ni 2p XPS spectra of Ni_1-N-C (X) (X = Cl, Br, and I). (b) Ni K-edge XANES spectra and (c) FT-EXAFS spectra of Ni foil and Ni_1-N-C (Cl). (d) EXAFS fitting of Ni_1-N-C (Cl) (inset: optimized coordination environment of Ni atom).

the carbon support, manifesting the atomic dispersion of Ni (Fig. 2(f)). The above results initially confirm the formation of single-atom Ni sites coordinated by nitrogen and the corresponding halogen atoms.

Furthermore, X-ray absorption spectroscopy (XAS) is employed to give more clear evidence on the coordination environments and electronic states of Ni atoms in Ni_1-N-C (X) (X = Cl, Br, and I) catalysts. It can be observed that the near-edge absorption energy of Ni_1-N-C (Cl) shifts to higher value compared with Ni foil in the Ni K-edge X-ray absorption near-edge structure (XANES) spectrum, indicating the positive valence state of Ni in Ni_1-N-C (Cl) (Fig. 3(b)). The Fourier transform-extended X-ray absorption fine structure (FT-EXAFS) curve of Ni_1-N-C (Cl) exhibits the dominated peak centered at ~ 1.60 Å, which could be attributed to the Ni-N/Cl coordination (Fig. 3(c)). In addition, the absence of Ni–Ni scattering path (around 2.18 Å) suggests the atomic dispersion of Ni atoms in Ni_1-N-C (Cl), agreeing well with the results of HAADF-STEM observation (Figs. 3(c) and 2(f)). Moreover, the EXAFS curve fitting is further performed to acquire the coordination configuration of Ni atoms of Ni_1-N-C (Cl). The best fitting result demonstrates that the Ni atom is coordinated with four in-plane N atoms and an axial Cl atom (Fig. 3(d) and Table S2 in the ESM). In addition, the XAS analysis has also been performed on Ni_1-N-C (Br) and Ni_1-N-C (I). The Ni K-edge XANES spectra of Ni_1-N-C (Br) and Ni_1-N-C (I) suggest the positive valence states of Ni in the two samples (Figs. S10(a) and S10(b) in the ESM). Furthermore, the best EXAFS curve fitting results for Ni_1-N-C (Br) and Ni_1-N-C (I) show their similar

coordination configurations to Ni_1-N-C (Cl), in which Ni atom is coordinated with four in-plane N atoms and an axial Br or I atom (Fig. S11 and Table S2 in the ESM).

Inspired by the results above, electrocatalytic CO_2 reduction measurements have been conducted using Ni_1-N-C (X) (X = Cl, Br, and I) as electrocatalysts. The linear sweep voltammetry (LSV) curves indicate that the current densities of Ni_1-N-C (X) (X = Cl, Br, and I) and N-C in CO_2 atmosphere are all higher than those in argon, manifesting their favorable activity for CO_2 reduction reaction (CO_2RR) (Figs. S12–S15 in the ESM). In addition, the current response of Ni_1-N-C (Cl) in CO_2 atmosphere is much higher than those of Ni_1-N-C (Br), Ni_1-N-C (I), and N-C (Fig. 4(a) and Fig. S15 in the ESM). When tested at constant potentials, Ni_1-N-C (Cl) shows the supreme CO FEs in all potentials ranging from −0.45 to −0.85 V (vs. RHE) (Fig. 4(b)). Significantly, Ni_1-N-C (Cl) affords a maximum CO FE of 94.7% at −0.7 V, outperforming those of Ni_1-N-C (Br) (83.3% at −0.65 V), Ni_1-N-C (I) (69.4% at −0.65 V), and N-C (57.1% at −0.55 V) (Fig. 4(b) and Fig. S16 in the ESM). For all tested catalysts, CO and H_2 are the main products, and no liquid products are identified from the ^{1}H nuclear magnetic resonance (^{1}H NMR) results (Fig. 4(b) and Figs. S16–S18 in the ESM). Additionally, Ni_1-N-C (Cl) also exhibits a superior CO partial current density (J_{CO}) to those of Ni_1-N-C (Br) and Ni_1-N-C (I), further manifesting excellent CO_2RR performance of Ni_1-N-C (Cl) (Fig. 4(c)). The Tafel slope of Ni_1-N-C (Cl) is 194 mV/dec, lower than those of Ni_1-N-C (Br) (209 mV/dec) and Ni_1-N-C (I) (252 mV/dec), revealing the fastest kinetics of Ni_1-N-C (Cl) for CO_2RR (Fig. S19 in the ESM). The double-layer capacitances (C_{dl}) are determined to be 28.9, 28.4, and 28.0 mF/cm^2 for Ni_1-N-C (Cl), Ni_1-N-C (Br), and Ni_1-N-C (I), respectively, indicating their similar electrochemical active surface area (ECSA) (Fig. S20 in the ESM). The similar ECSA as well as Ni loading of different samples further prove that the catalytic performance difference of Ni_1-N-C (Cl), Ni_1-N-C (Br), and Ni_1-N-C (I) is actually caused by the different axial halide atoms (Fig. S20 and Table S1 in the ESM). Finally, the stability measurement of best-performed Ni_1-N-C (Cl) is conducted at −0.7 V, and it can be seen that the FE of CO and current densities can be well retained during 10 h, demonstrating the long-term stability of Ni_1-N-C (Cl) for CO_2RR (Fig. 4(d)).

Given the superb CO_2RR performance of Ni_1-N-C (Cl), it is further employed as a cathode catalyst in the rechargeable Zn-CO_2 battery [51, 55]. The Ni_1-N-C (Cl) is immersed in 0.8 M CO_2-saturated $KHCO_3$ electrolyte. The Zn foil, serving as the anode, is put in 0.8 M KOH solution containing 0.02 M $Zn(CH_3COO)_2$ (Fig. 5(a)). During the discharge process, the cathode reaction is CO_2 reduction and the Zn anode converts into $Zn(OH)_4^{2-}$ [55]. In the charge process, oxygen forms on the cathode and the anode reaction is the deposition of Zn [55]. As shown in the discharge and charge voltage profiles, Ni_1-N-C (Cl) exhibits a discharge potential of 0.426 V at 0.5 mA, which still maintains at 0.175 V when 2.5 mA discharge current is applied (Fig. 5(b)). In the meantime, a charge potential of 2.257 V results from a charge current of 0.5 mA, which increases slowly after 1 mA (Fig. 5(b)). Meanwhile, the selectivity of CO reaches 93.8% at 2 mA during the discharge process and can be well retained in a wide range of discharge current, indicating the excellent CO_2 reduction performance of Ni_1-N-C (Cl) (Fig. 5(c)). Moreover, Ni_1-N-C (Cl) displays stable voltage under consecutively discharge/charge at 2.0 mA/cm^2 for 24 h, suggesting the excellent stability of the Zn-CO_2 cell (Fig. 5(d)).

To uncover the influence of axial coordination environments on the CO_2RR performance of single Ni atoms, density functional theory (DFT) calculations are further implemented (Fig. S21 in the ESM). As shown in the charge density difference in the three samples, more electrons transfer from Ni to the axial Cl than Br and I, which is consistent with the results based on Bader charge analysis (Fig. S22 and Table S3 in the ESM). The different electron delocalization degree of Ni atoms caused by halogen atoms with different electronegativity will also affect the reaction energy barriers. To prove this, the free-energy change (ΔG) for CO_2 reduction to CO has been calculated (Fig. S23 in the ESM). Usually, the formation of *COOH is regarded as the rate-limiting step [56–58]. The ΔG for the *COOH formation on Ni_1-N-C (Cl) is determined to be 1.78 eV, smaller than those on Ni_1-N-C (Br) (1.86 eV) and Ni_1-N-C (I) (1.90 eV), demonstrating the lowest

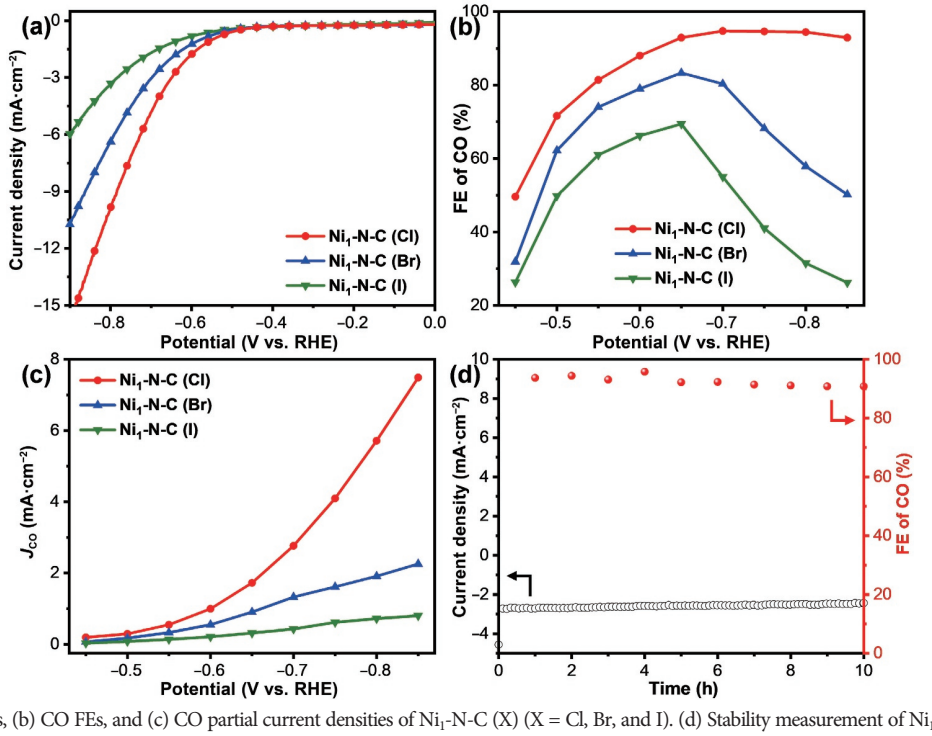

Figure 4 (a) LSV curves, (b) CO FEs, and (c) CO partial current densities of Ni_1-N-C (X) (X = Cl, Br, and I). (d) Stability measurement of Ni_1-N-C (Cl) at −0.7 V vs. RHE in CO_2-saturated 0.5 M $KHCO_3$.

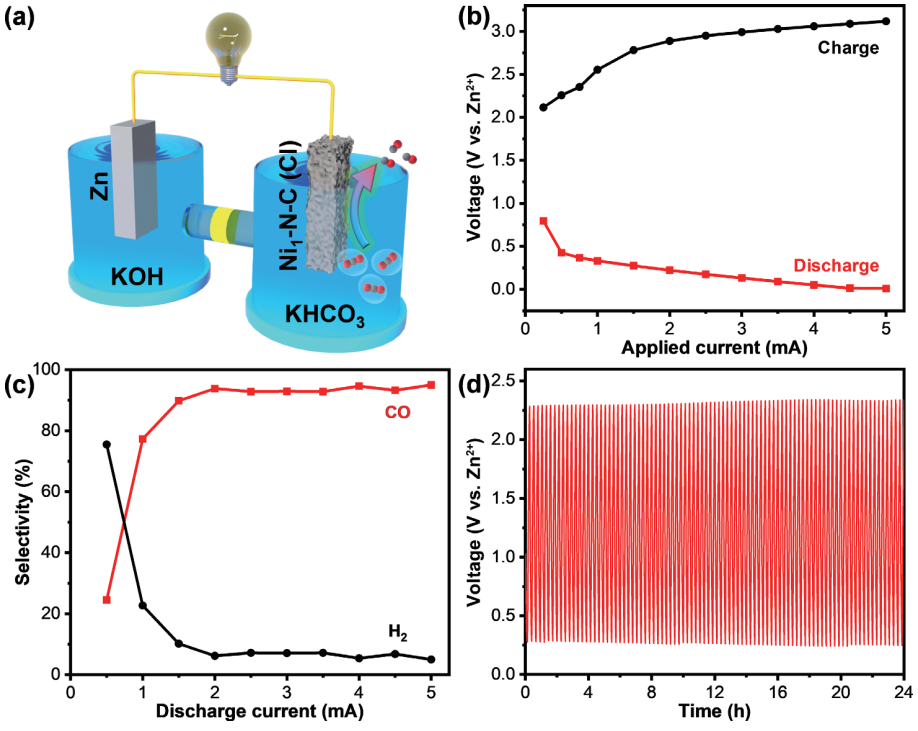

Figure 5 (a) Schematic illustration of the Zn-CO_2 battery with Ni_1-N-C (Cl) cathode. (b) Discharge and charge voltage profiles for Zn-CO_2 battery. (c) Selectivity of Ni_1-N-C (Cl) for CO and H_2 under different discharge current densities. (d) Galvanostatic discharge–charge cycling curves at 2.0 mA/cm² for 24 h.

energy barrier of Ni_1-N-C (Cl) for CO_2RR (Fig. 6(a) and Fig. S24 in the ESM). Electron localization function (ELF) images exhibit the high degree of electron localization between single-atom Ni in Ni_1-N-C (Cl) and *COOH intermediate, while there is little localized electron between single-atom Ni and *CO, suggesting the strong interaction of Ni_1-N-C (Cl) with *COOH and weak interaction with *CO (Fig. 6(b)). Moreover, Ni_1-N-C (Cl) possesses the shortest distance between absorbed *COOH and central Ni atom, and the largest *COOH adsorption energy, further supporting the superior performance of Ni_1-N-C (Cl) for CO_2RR, in accordance with the experimental results (Fig. 6(c)).

3 Conclusions

In summary, a straightforward and facile PMHM method is put forward to fabricate single-atom Ni catalysts coordinated with nitrogen and halogen atoms. By simply adjusting the halogen anions of the nickel salts in the single atom decoration process, a series of single-atom Ni catalysts with different axial coordinated halogen atoms (Ni_1-N-C (X), X = Cl, Br, and I) are rationally constructed. The axial coordinated halogen atoms, with different electronegativity, can significantly regulate the electronic states of the single metal atoms. When performed as an electrocatalyst for CO_2 reduction, the obtained Ni_1-N-C (Cl) catalyst, with the single atom Ni coordinated by four N atoms and an axial Cl atom, manifests outstanding CO_2RR performance with ultrahigh CO FE up to 94.7%, far surpassing Ni_1-N-C (Br) and Ni_1-N-C (I). Moreover, when employed as a cathode catalyst in the Zn-CO_2 battery, Ni_1-N-C (Cl) also exhibits ultrahigh selectivity for CO and long-term stability. Theoretical calculations reveal that Ni_1-N-C (Cl) with the most electronegative Cl coordination in the axial direction could reduce the formation barrier of *COOH, thus boosting the CO_2RR performance. This work presents a facile and universal strategy for the regulation of coordination environments

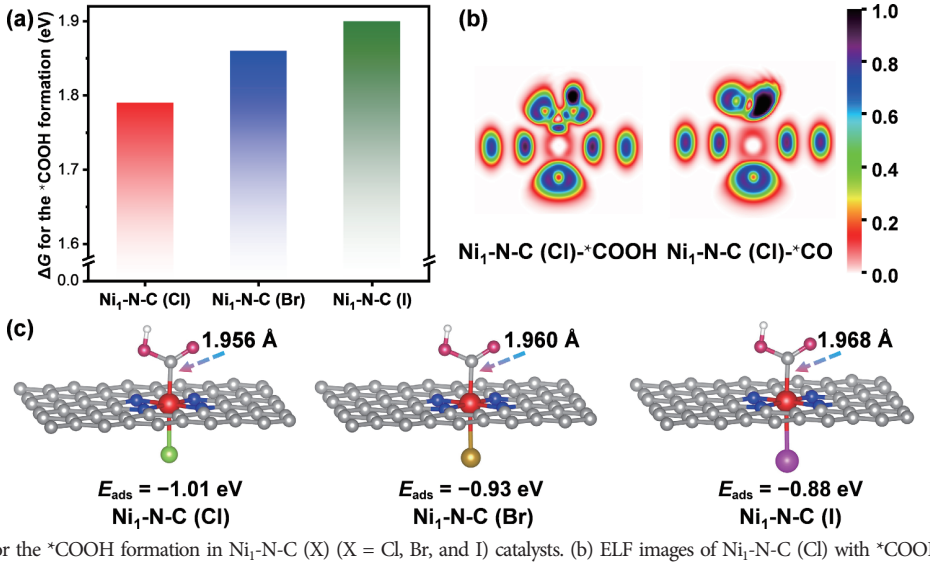

Figure 6 (a) The Δ*G* for the *COOH formation in Ni_1-N-C (X) (X = Cl, Br, and I) catalysts. (b) ELF images of Ni_1-N-C (Cl) with *COOH and *CO adsorption. (c) The DFT-optimized configurations of Ni_1-N-C (X) (X = Cl, Br, and I) with *COOH adsorption and corresponding adsorption energy.

and brings great opportunities for the catalytic performance optimization of single-atom catalysts.

Acknowledgements

This work was supported by the National Key Research and Development Program of China (No. 2021YFA1500402), the National Natural Science Foundation of China (NSFC) (Nos. 21725101, 21871244, and 22001242), International Partnership Program of Chinese Academy of Sciences (CAS) (No. 211134KYSB20190109), Collaborative Innovation Program of Hefei Science Center, CAS (No. 2020HSC-CIP005), and the Fundamental Research Funds for the Central Universities (Nos. WK2060000038 and WK2060000040). We thank the XAFS measurements from 1W1B station at BSRF.

Electronic Supplementary Material: Supplementary material (materials and instrumentation, experimental section, electrochemical measurements, the details for X-ray adsorption spectra and Zn-CO_2 battery, computational details, XRD results, N_2 sorption isotherm, Raman spectra, SEM and TEM images, XPS spectra, XAFS results, electrochemical results, ^{1}H NMR spectra, DFT calculation results, and the element contents for N and Ni) is available in the online version of this article at https://doi.org/10.1007/s12274-022-4467-3.

References

[1] Wang, A. Q.; Li, J.; Zhang, T. Heterogeneous single-atom catalysis. *Nat. Rev. Chem.* **2018**, *2*, 65–81.

[2] Chen, Y. J.; Ji, S. F.; Chen, C.; Peng, Q.; Wang, D. S.; Li, Y. D. Single-atom catalysts: Synthetic strategies and electrochemical applications. *Joule* **2018**, *2*, 1242–1264.

[3] Liu, L. C.; Corma, A. Metal catalysts for heterogeneous catalysis: From single atoms to nanoclusters and nanoparticles. *Chem. Rev.* **2018**, *118*, 4981–5079.

[4] Fei, H. L.; Dong, J. C.; Chen, D. L.; Hu, T. D.; Duan, X. D.; Shakir, I.; Huang, Y.; Duan, X. F. Single atom electrocatalysts supported on graphene or graphene-like carbons. *Chem. Soc. Rev.* **2019**, *48*, 5207–5241.

[5] Zhu, C. Z.; Fu, S. F.; Shi, Q. R.; Du, D.; Lin, Y. H. Single-atom electrocatalysts. *Angew. Chem., Int. Ed.* **2017**, *56*, 13944–13960.

[6] Li, X. N.; Yang, X. F.; Huang, Y. Q.; Zhang, T.; Liu, B. Supported noble-metal single atoms for heterogeneous catalysis. *Adv. Mater.* **2019**, *31*, 1902031.

[7] Yi, J. D.; Xu, R.; Wu. Q.; Zhang, T.; Zang, K. T.; Luo, J.; Liang, Y. L.; Huang, Y. B.; Cao, R. Atomically dispersed iron-nitrogen active sites within porphyrinic triazine-based frameworks for oxygen reduction reaction in both alkaline and acidic media. *ACS Energy Lett.* **2018**, *3*, 883–889.

[8] Yang, S. X.; Yu, Y. H.; Dou, M. L.; Zhang, Z. P.; Dai, L. M.; Wang, F. Two-dimensional conjugated aromatic networks as high-site-density and single-atom electrocatalysts for the oxygen reduction reaction. *Angew. Chem., Int. Ed.* **2019**, *58*, 14724–14730.

[9] Zhang, J.; Wang, Y. X.; Yang, C. J.; Chen, S. A.; Li, Z. J.; Cheng, Y.; Wang, H. N.; Xiang, Y.; Lu, S. F.; Wang, S. Y. Elucidating the electro-catalytic oxidation of hydrazine over carbon nanotube-based transition metal single atom catalysts. *Nano Res.* **2021**, *14*, 4650–4657.

[10] Lin, L. L.; Yu, Q. L.; Peng, M.; Li, A. W.; Yao, S. Y.; Tian, S. H.; Liu, X.; Li, A.; Jiang, Z.; Gao, R. et al. Atomically dispersed Ni/α-MoC catalyst for hydrogen production from methanol/water. *J. Am. Chem. Soc.* **2021**, *143*, 309–317.

[11] Qi, K.; Chhowalla, M.; Voiry, D. Single atom is not alone: Metal–support interactions in single-atom catalysis. *Mater. Today* **2020**, *40*, 173–192.

[12] Qin, R. X.; Liu, K. L.; Wu, Q. Y.; Zheng, N. F. Surface coordination chemistry of atomically dispersed metal catalysts. *Chem. Rev.* **2020**, *120*, 11810–11899.

[13] Li, X. Y.; Rong, H. P.; Zhang, J. T.; Wang, D. S.; Li, Y. D. Modulating the local coordination environment of single-atom catalysts for enhanced catalytic performance. *Nano Res.* **2020**, *13*, 1842–1855.

[14] Zhu, Y. Z.; Sokolowski, J.; Song, X. C.; He, Y. H.; Mei, Y.; Wu, G. Engineering local coordination environments of atomically dispersed and heteroatom-coordinated single metal site electrocatalysts for clean energy-conversion. *Adv. Energy Mater.* **2020**, *10*, 1902844.

[15] Yang, Q.; Jia, Y.; Wei, F. F.; Zhuang, L. Z.; Yang, D. J.; Liu, J. Z.; Wang, X.; Lin, S.; Yuan, P.; Yao, X. D. Understanding the activity of Co-$N_{4-x}C_x$ in atomic metal catalysts for oxygen reduction catalysis. *Angew. Chem., Int. Ed.* **2020**, *59*, 6122–6127.

[16] Sun, X. H.; Tuo, Y. X.; Ye, C. L.; Chen, C.; Lu. Q.; Li, G. N.; Jiang, P.; Chen, S. H.; Zhu, P.; Ma, M. et al. Phosphorus induced electron localization of single iron sites for boosted CO_2 electroreduction reaction. *Angew. Chem., Int. Ed.* **2021**, *60*, 23614–23618.

[17] Rong, X.; Wang, H. J.; Lu, X. L.; Si, R.; Lu, T. B. Controlled synthesis of a vacancy-defect single-atom catalyst for boosting CO_2 electroreduction. *Angew. Chem., Int. Ed.* **2020**, *59*, 1961–1965.

[18] Daiyan, R.; Zhu, X. F.; Tong, Z. Z.; Gong, L. L.; Razmjou, A.; Liu, R. S.; Xia, Z. H.; Lu, X. Y.; Dai, L. M.; Amal, R. Transforming active sites in nickel-nitrogen-carbon catalysts for efficient electrochemical CO_2 reduction to CO. *Nano Energy* **2020**, *78*, 105213.

[19] Gao, D. F.; Liu, T. F.; Wang, G. X.; Bao, X. H. Structure sensitivity in single-atom catalysis toward CO_2 electroreduction. *ACS Energy Lett.* **2021**, *6*, 713–727.

[20] Wang, Y.; Zheng, X. B.; Wang, D. S. Design concept for electrocatalysts. *Nano Res.* **2022**, *15*, 1730–1752.

[21] Jing, H. Y.; Zhu, P.; Zheng, X. B.; Zhang, Z. D.; Wang, D. S.; Li, Y. D. Theory-oriented screening and discovery of advanced energy transformation materials in electrocatalysis. *Adv. Powder Mater.* **2022**, *1*, 100013.

[22] Tang, C.; Chen, L.; Li, H. J.; Li, L. Q.; Jiao, Y.; Zheng, Y.; Xu, H. L.; Davey, K.; Qiao, S. Z. Tailoring acidic oxygen reduction selectivity on single-atom catalysts via modification of first and second coordination spheres. *J. Am. Chem. Soc.* **2021**, *143*, 7819–7827.

[23] Varela, A. S.; Ju, W.; Bagger, A.; Franco, P.; Rossmeisl, J.; Strasser, P. Electrochemical reduction of CO_2 on metal-nitrogen-doped carbon catalysts. *ACS Catal.* **2019**, *9*, 7270–7284.

[24] Yang, H. Z.; Shi, R.; Shang, L.; Zhang, T. R. Recent advancements of porphyrin-like single-atom catalysts: Synthesis and applications. *Small Struct.* **2021**, *2*, 2100007.

[25] Huang, M.; Deng, B. W.; Zhao, X. L.; Zhang, Z. Y.; Li, F.; Li, K. L.; Cui, Z. H.; Kong, L. X.; Lu, J. M; Dong, F. et. al. Template-sacrificing synthesis of well-defined asymmetrically coordinated single-atom catalysts for highly efficient CO_2 electrocatalytic reduction. *ACS Nano* **2022**, *16*, 2110–2119.

[26] Jing, H. Y.; Liu, W.; Zhao, Z. Y.; Zhang, J. W.; Zhu, C.; Shi, Y. T.; Wang, D. S.; Li, Y. D. Electronics and coordination engineering of atomic cobalt trapped by oxygen-driven defects for efficient cathode in solar cells. *Nano Energy* **2021**, *89*, 106365.

[27] Jing, H. Y.; Zhao, Z. Y.; Zhang, J. W.; Zhu, C.; Liu, W.; Li, N. N.; Hao, C.; Shi, Y. T.; Wang, D. S. Atomic evolution of metal–organic frameworks into Co–N_3 coupling vacancies by cooperative cascade protection strategy for promoting triiodide reduction. *J. Phys. Chem. C* **2021**, *125*, 6147–6156.

[28] Zhi, Q. J.; Jiang, R.; Liu, W. P.; Sun, T. T.; Wang, K.; Jiang, J. Z. Atomic CoN_3S_1 sites for boosting oxygen reduction reaction via an atomic exchange strategy. *Nano Res.* **2022**, *15*, 1803–1808.

[29] Gong, Y. N.; Jiao, L.; Qian, Y. Y.; Pan, C. Y.; Zheng, L. R.; Cai, X. C.; Liu, B.; Yu, S. H.; Jiang, H. L. Regulating the coordination environment of MOF-templated single-atom nickel electrocatalysts for boosting CO_2 reduction. *Angew. Chem., Int. Ed.* **2020**, *59*, 2705–2709.

[30] Pan, Y.; Chen, Y. J.; Wu, K. L.; Chen, Z.; Liu, S. J.; Cao, X.; Cheong, W. C.; Meng, T.; Luo, J.; Zheng, L. R. et al. Regulating the coordination structure of single-atom Fe-N_xC_y catalytic sites for benzene oxidation. *Nat. Commun.* **2019**, *10*, 4290.

[31] Zhao, C. X.; Li, B. Q.; Liu, J. N.; Zhang, Q. Intrinsic electrocatalytic activity regulation of M-N-C single-atom catalysts for the oxygen reduction reaction. *Angew. Chem., Int. Ed.* **2021**, *60*, 4448–4463.
[32] Wang, X. Y.; Wang, Y.; Sang, X. H.; Zheng, W. Z.; Zhang, S. H.; Shuai, L.; Yang, B.; Li, Z. J.; Chen, J. M.; Lei, L. C. et al. Dynamic activation of adsorbed intermediates via axial traction for the promoted electrochemical CO_2 reduction. *Angew. Chem., Int. Ed.* **2021**, *60*, 4192–4198.
[33] Chen, Z. Q.; Huang, A. J.; Yu, K.; Cui, T. T.; Zhuang, Z. W.; Liu, S. J.; Li, J. Z.; Tu, R. Y.; Sun, K. A.; Tan, X. et al. Fe_1N_4-O_1 site with axial Fe-O coordination for highly selective CO_2 reduction over a wide potential range. *Energy Environ. Sci.* **2021**, *14*, 3430–3437.
[34] Furukawa, H.; Cordova, K. E.; O'Keeffe, M.; Yaghi, O. M. The chemistry and applications of metal–organic frameworks. *Science,* **2013**, *341*, 1230444.
[35] Zhou, H. C. J.; Kitagawa, S. Metal–organic frameworks (MOFs). *Chem. Soc. Rev.* **2014**, *43*, 5415–5418.
[36] Islamoglu, T.; Goswami, S.; Li, Z. Y.; Howarth, A. J.; Farha, O. K.; Hupp, J. T. Postsynthetic tuning of metal–organic frameworks for targeted applications. *Acc. Chem. Res.* **2017**, *50*, 805–813.
[37] Cai, G. R.; Yan, P.; Zhang, L. L.; Zhou, H. C.; Jiang, H. L. Metal–organic framework-based hierarchically porous materials: Synthesis and applications. *Chem. Rev.* **2021**, *121*, 12278–12326.
[38] Lin, R. B.; Xiang, S. C.; Zhou, W.; Chen, B. L. Microporous metal–organic framework materials for gas separation. *Chem* **2020**, *6*, 337–363.
[39] Qiu, T. J.; Liang, Z. B.; Guo, W. H.; Tabassum, H.; Gao, S.; Zou, R. Q. Metal–organic framework-based materials for energy conversion and storage. *ACS Energy Lett.* **2020**, *5*, 520–532.
[40] Li, X. R.; Yang, X. C.; Xue, H. G.; Pang, H.; Xu, Q. Metal–organic frameworks as a platform for clean energy applications. *EnergyChem* **2020**, *2*, 100027.
[41] Chen, Y. Z.; Zhang, R.; Jiao, L.; Jiang, H. L. Metal–organic framework-derived porous materials for catalysis. *Coord. Chem. Rev.* **2018**, *362*, 1–23.
[42] Zhao, S. L.; Tan, C. H.; He, C. T.; An, P. F.; Xie, F.; Jiang, S.; Zhu, Y. F.; Wu, K. H.; Zhang, B. W.; Li, H. J. et al. Structural transformation of highly active metal–organic framework electrocatalysts during the oxygen evolution reaction. *Nat. Energy* **2020**, *5*, 881–890.
[43] Chen, S. H.; Li, W. H.; Jiang, W. J.; Yang, J. R.; Zhu, J. X.; Wang, L. Q.; Ou, H. H.; Zhuang, Z. C.; Chen, M. Z.; Sun, X. H. et al. MOF encapsulating N-heterocyclic carbene-ligated copper single-atom site catalyst towards efficient methane electrosynthesis. *Angew. Chem., Int. Ed.* **2022**, *61*, e202114450.
[44] Wei, Y. S.; Zhang, M.; Zou, R. Q.; Xu. Q. Metal–organic framework-based catalysts with single metal sites. *Chem. Rev.* **2020**, *120*, 12089–12174.
[45] Yang, H. P.; Wu, Y.; Li, G. D.; Lin, Q.; Hu, Q.; Zhang, Q. L.; Liu, J. H.; He, C. X. Scalable production of efficient single-atom copper decorated carbon membranes for CO_2 electroreduction to methanol. *J. Am. Chem. Soc.* **2019**, *141*, 12717–12723.
[46] Guan, A. X.; Chen, Z.; Quan, Y. L.; Peng, C.; Wang, Z. Q.; Sham, T. K.; Yang, C.; Ji, Y. L.; Qian, L. P.; Xu, X. et al. Boosting CO_2 electroreduction to CH_4 via tuning neighboring single-copper sites. *ACS Energy Lett.* **2020**, *5*, 1044–1053.
[47] Stavretis, S. E.; Atanasov, M.; Podlesnyak, A. A.; Hunter, S. C.; Neese, F.; Xue, Z. L. Magnetic transitions in iron porphyrin halides by inelastic neutron scattering and *ab initio* studies of zero-field splittings. *Inorg. Chem.* **2015**, *54*, 9790–9801.
[48] Huang, X. C.; Lin, Y. Y.; Zhang, J. P.; Chen, X. M. Ligand-directed strategy for zeolite-type metal–organic frameworks: Zinc(Ⅱ) imidazolates with unusual zeolitic topologies. *Angew. Chem., Int. Ed.* **2006**, *45*, 1557–1559.
[49] Park, K. S.; Ni, Z.; Côté, A. P.; Choi, J. Y.; Huang, R. D.; Uribe-Romo, F. J.; Chae, H. K.; O'Keeffe, M.; Yaghi, O. M. Exceptional chemical and thermal stability of zeolitic imidazolate frameworks. *Proc. Natl. Acad. Sci. USA.* **2006**, *103*, 10186–10191.
[50] Matienzo, J.; Yin, L. I.; Grim, S. O.; Swartz, W. E. Jr. X-ray photoelectron spectroscopy of nickel compounds. *Inorg. Chem.* **1973**, *12*, 2762–2769.
[51] Jiao, L.; Zhu, J. T.; Zhang, Y.; Yang, W. J.; Zhou, S. Y.; Li, A. W.; Xie, C. F.; Zheng, X. S.; Zhou, W.; Yu, S. H. et al. Non-bonding interaction of neighboring Fe and Ni single-atom pairs on MOF-derived N-doped carbon for enhanced CO_2 electroreduction. *J. Am. Chem. Soc.* **2021**, *143*, 19417–19424.
[52] Zhang, B. X.; Zhang, J. L.; Shi, J. B.; Tan, D. X.; Liu, L. F.; Zhang, F. Y.; Lu, C.; Su, Z. Z.; Tan, X. N.; Cheng, X. Y. et al. Manganese acting as a high-performance heterogeneous electrocatalyst in carbon dioxide reduction. *Nat. Commun.* **2019**, *10*, 2980.
[53] Zhang, Y. H.; Tang, Z. R.; Fu, X. Z.; Xu, Y. J. Nanocomposite of Ag-AgBr-TiO_2 as a photoactive and durable catalyst for degradation of volatile organic compounds in the gas phase. *Appl. Catal. B* **2011**, *106*, 445–452.
[54] Fan, Q.; Huang, J. W.; Dong, N. N.; Hong, S.; Yan, C.; Liu, Y. C.; Qiu, J. S.; Wang, J.; Sun, Z. Y. Liquid exfoliation of two-dimensional PbI_2 nanosheets for ultrafast photonics. *ACS Photonics* **2019**, *6*, 1051–1057.
[55] Xie, J. F.; Zhou, Z.; Wang, Y. B. Metal-CO_2 batteries at the crossroad to practical energy storage and CO_2 recycle. *Adv. Funct. Mater.* **2020**, *30*, 1908285.
[56] Liu, M.; Pang, Y. J.; Zhang, B.; Luna, P. D.; Voznyy, O.; Xu, J. X.; Zheng, X. L.; Dinh, C. T.; Fan, F. J.; Cao, C. H. et al. Enhanced electrocatalytic CO_2 reduction via field-induced reagent concentration. *Nature* **2016**, *537*, 382–386.
[57] Sun, S. N.; Li, N.; Liu, J.; Ji, W. X.; Dong, L. Z.; Wang, Y. R.; Lan Y. Q. Identification of the activity source of CO_2 electroreduction by strategic catalytic site distribution in stable supramolecular structure system. *Natl. Sci. Rev.* **2021**, *8*, nwaa195.
[58] Zheng, T. T.; Jiang, K.; Wang, H. T. Recent advances in electrochemical CO_2-to-CO conversion on heterogeneous catalysts. *Adv. Mater.* **2018**, *30*, 1802066.